Visible-spanning flat supercontinuum for astronomical applications

Aakash Ravi,[1,*] Matthias Beck,[2] David F. Phillips,[3] Albrecht Bartels,[2]
Dimitar Sasselov,[3] Andrew Szentgyorgyi,[3] and Ronald L. Walsworth[1,3]

[1] *Department of Physics, Harvard University, Cambridge, MA 02138, USA*
[2] *Laser Quantum GmbH, Max-Stromeyer-Str. 116, 78467 Konstanz, Germany*
[3] *Harvard-Smithsonian Center for Astrophysics, 60 Garden St., Cambridge, MA 02138, USA*

(Dated: July 23, 2018)

We demonstrate a broad, flat visible supercontinuum spectrum that is generated by a dispersion-engineered tapered photonic crystal fiber pumped by a 1 GHz repetition rate turn-key Ti:sapphire laser outputting ~ 30 fs pulses at 800 nm. At a pulse energy of 100 pJ, we obtain an output spectrum that is flat to within 3 dB over the range 490-690 nm with a blue tail extending below 450 nm. The mode-locked laser combined with the photonic crystal fiber forms a simple visible frequency comb system that is extremely well-suited to the precise calibration of astrophysical spectrographs, among other applications.

arXiv:1807.07857v1 [astro-ph.IM] 18 Jul 2018

INTRODUCTION

Doppler spectroscopy of stars using high-resolution astrophysical spectrographs enables the detection of exoplanets through measurement of periodic variations in the radial velocity of the host star [1]. Since such measurements are inherently photon-flux-limited and require spectral sensitivity much better than the resolution of the spectrograph, they require combining information from thousands of just-resolved spectral lines across the passband of the instrument. Doing this reliably over orbital timescales requires an extremely stable calibration source with a large bandwidth and uniform spectral coverage. State-of-the-art spectrographs used in Doppler exoplanet searches such as HARPS [2] and HARPS-N [3] operate in the visible wavelength range (400-700 nm). Laser frequency combs are well suited to calibrating these instruments, and several "astro-comb" designs have been successfully demonstrated to date (see Ref. [4] and references therein).

Existing astro-comb architectures are based on near-infrared source combs (e.g. Ti:sapphire, Yb/Er fiber), so providing visible calibration light for an astrophysical spectrograph typically requires a nonlinear optical element to coherently shift and broaden the source comb radiation. Early astro-combs derived from Ti:sapphire source combs relied on second harmonic generation [5, 6] but had limited utility due to extremely low output bandwidth ($\sim$ 15 nm). This is a serious shortfall because the exoplanet detection sensitivity depends on the bandwidth of the observed stellar light that is calibrated. A calibration source with a larger bandwidth can therefore enable more precise determination of stellar Doppler shifts. A better alternative to frequency doubling is to pump a highly nonlinear photonic crystal fiber (PCF) with the source comb to take advantage of supercontinuum generation [7], an effect where a narrowband high-intensity pulse experiences extreme spectral broadening as a result of interactions with the medium through which it propagates. The dispersion and nonlinearity of PCFs may be engineered via suitable changes in geometry; for example, two commonly used parameters are the pitch and the diameter of the air holes. PCFs also typically exhibit very high nonlinearities compared to standard optical fibers due to their small effective mode field diameters. As a result of these attractive properties, broadband supercontinuum generation using PCFs has found many applications, from optical coherence tomography [8] to carrier-envelope-phase stabilization of femtosecond lasers [9], as well as calibration of astrophysical spectrographs [10–14]. Beyond spectral bandwidth, another property that is desired for astronomical calibration applications is spectral flatness, i.e., low intensity variation across the band of the calibration source. Spectral flatness is valued because calibration precision is both shot-noise- and CCD-saturation-limited. Therefore the largest photoelectron count below CCD saturation per exposure provides the optimal calibration. This condition is best fulfilled for a uniform intensity distribution over all the comb peaks [11].

In the present work, we show that careful dispersion-engineering of a PCF by tapering enables the production of a very broad, flat, and high-intensity optical supercontinuum spectrum from pump radiation emitted by a turn-key Ti:sapphire comb. Previous attempts to produce such a supercontinuum from a Ti:sapphire comb have reported relatively low spectral coverage (500-620 nm) and large intensity variations ($\sim$ 10 dB) across the band [13]. A flat 235 nm-wide visible supercontinuum has been demonstrated using a Yb:fiber comb [15], but at the expense of greater system complexity and losses incurred by spectral flattening using a spatial light modulator [11].

FIBER GEOMETRY AND PARAMETERS

In our application, we consider a PCF with a 2.8 µm core diameter and a 850 nm zero dispersion wavelength

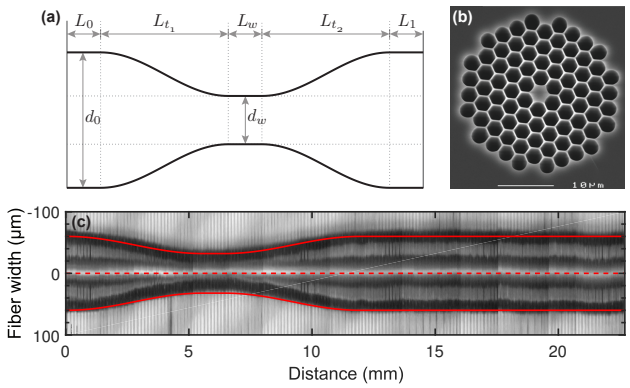


Figure 1. (a) General tapered photonic crystal fiber (PCF) geometry showing varying core size vs. length. The quantities d_0, d_w, $L_{0,1}$, $L_{t_{1,2}}$, and L_w parametrize the geometry; see text for details. (b) SEM micrograph (courtesy of NKT Photonics A/S) of end face of raw NL-2.8-850-02 PCF. (c) Composite microscope image of fabricated tapered PCF. Overlaid red curves represent the proposed geometry, scaled by the cladding/core size ratio.

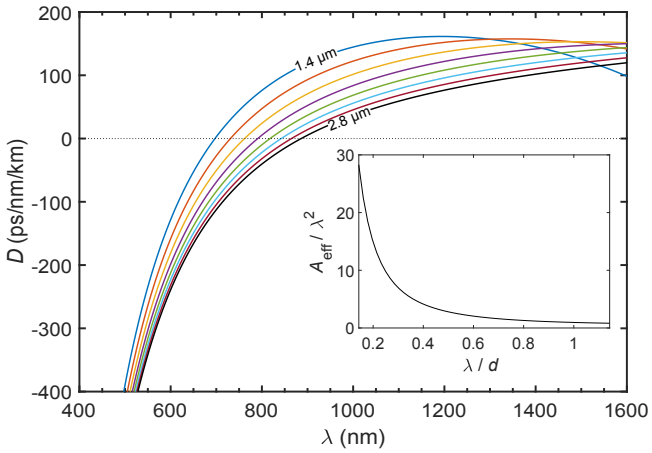


Figure 2. Simulated PCF properties. Main plot: chromatic dispersion curves for varying core diameter d (curves spaced apart by $\Delta d = 0.2$ μm). Inset: Normalized effective area vs. normalized wavelength.

(NKT Photonics NL-2.8-850-02). The cross section of the fiber is shown in Figure 1b. We chose a large core diameter to facilitate coupling and have the zero dispersion wavelength (ZDW) near our 800 nm pump wavelength. Changing the PCF core diameter as a function of distance along the fiber via tapering modifies both the dispersion and nonlinearity of the PCF. Sometimes termed "dispersion micromanagement" in the literature, such techniques have been pursued before with PCFs to enable generation of light with increased bandwidth and flatness [16–19], but not targeted specifically toward uniform visible wavelength coverage using GHz repetition rate lasers.

To design a device capable of producing a flat visible-spanning spectrum when pumped with 800 nm femtosecond pulses, we model optical pulse propagation in the PCF by solving the generalized nonlinear Schrödinger equation (GNLSE) as outlined in Appendix A. In our design, we consider a specific taper geometry, as shown in Figure 1a. The core diameter d changes smoothly over the tapers with a cosine function $d(\zeta) = d_i + \frac{1}{2}(1 - \cos\pi\zeta)(d_f - d_i)$ over $\zeta \in [0, 1]$, where d_i and d_f are, respectively, the initial and final core diameters of the down- or up-taper. The nondimensionalized variable ζ parametrizes the distance along the taper, i.e., $\zeta = (z - L_0)/L_{t_1}$ or $\zeta = (z - (L_0 + L_{t_1} + L_w))/L_{t_2}$.

Over the desired range of core diameters (1.4 μm $\leq d \leq$ 2.8 μm), we compute the PCF dispersion and nonlinearity as inputs for the pulse propagation calculations. We use a commercial finite-difference mode solver (Lumerical MODE Solutions) to calculate the PCF properties. Figure 2 shows the chromatic dispersion $D = -\frac{\omega^2}{2\pi c}\frac{\partial^2\beta}{\partial\omega^2}$ versus wavelength λ as a function of core diameter d (β is the propagation constant of the fundamental mode and ω is the angular frequency of light). Additionally, the inset of Figure 2 shows the modal area A_{eff} calculation for the PCF. This calculation is required only for a single core diameter because A_{eff} respects the scale invariance of Maxwell's equations, as pointed out in Ref. [20], whereas dispersion does not. In subsequent results where we solve the GNLSE in a tapered PCF, the dispersion was interpolated to the local fiber diameter from a pre-computed set of dispersion curves spaced apart by $\Delta d = 0.05$ μm. In addition, the effective area was evaluated for each PCF diameter according to the computed curve in terms of the normalized variables shown in the inset of Figure 2.

TAPERED FIBER DESIGN

We design a taper geometry for our PCF with the following parameters: $d_0 = 2.8$ μm, $d_w = 1.5$ μm, $L_0 = 50$ μm, $L_{t_1} = L_{t_2} = 5.5$ mm, $L_w = 900$ μm and $L_1 = 9.55$ mm, as shown in Figure 3a. These geometric parameters were manually chosen to produce a supercontinuum with low intensity variation in the visible wavelength range while trying to push the blue edge of the supercontinuum to wavelengths as short as possible. A design derived using an optimization method with a merit function capturing these desired qualities may lead to enhanced performance, but is outside the scope of this work.

The pump radiation for the PCF is sourced from a taccor comb (Laser Quantum). This system is a turnkey 1 GHz Ti:sapphire mode-locked laser with repetition rate and carrier-envelope offset stabilization. The comb center wavelength is $\sim$ 800 nm and the laser output bandwidth is approximately 35 nm, so the transform-limited intensity full width at half maximum (FWHM)

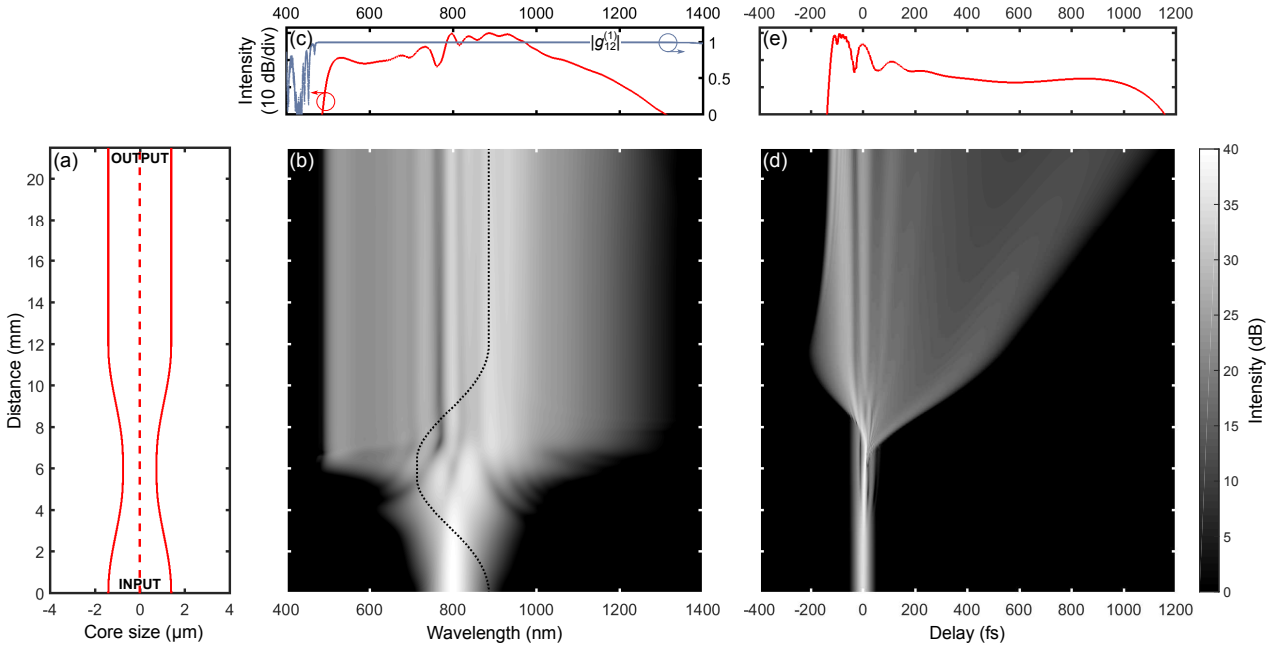


Figure 3. Simulated spectral and temporal evolution in a tapered PCF of a 210 pJ, 19.5 fs hyperbolic secant pulse at 800 nm. (a) PCF core size vs. longitudinal distance (0 is the fiber input face). (b) Pulse evolution vs. distance in the spectral (wavelength) domain. The PCF's computed zero dispersion wavelength (ZDW) is superimposed as a dotted black curve. (c) Pulse spectrum and magnitude of the first-order coherence $g_{12}^{(1)}$ at the fiber output face (d) Pulse evolution vs. distance in the time domain. (e) Pulse time trace at fiber output face.

is 27 fs for a Gaussian pulse shape (19.5 fs for a hyperbolic secant pulse shape).

By integrating the GNLSE (see Appendix A) with a fourth-order Runge-Kutta method, we investigate idealized pulse evolution in the tapered PCF assuming an initial hyperbolic secant pulse shape of the form $\sqrt{P_0}\mathrm{sech}\,(T/T_0)$. Here $T_0 \approx T_{\mathrm{FWHM}}/1.76$, $P_0 \approx 0.88E_p/T_{\mathrm{FWHM}}$ is the pulse peak power, and E_p is the pulse energy. Figure 3b and d show the pulse spectral and temporal evolution, respectively for $E_p = 210$ pJ evolving in the tapered PCF, whose geometry is represented in Figure 3a. Panels c and e show the spectrum and time traces of the pulse at the fiber output. Panel c also shows the magnitude of the first-order coherence $g_{12}^{(1)}$ of the output (see Appendix B for more details). Focusing on the panels b and d, we see that the initial dynamics correspond to symmetric spectral broadening and an unchanged temporal envelope associated with self-phase modulation [21]. This is because the pump pulse is initially propagating in the normal dispersion regime (i.e., chromatic dispersion $D < 0$). As the PCF narrows, the pulse crosses over into the anomalous ($D > 0$) dispersion regime. Here, perturbations such as higher-order dispersion and Raman scattering induce pulse break-up in a process called soliton fission [21]. Subsequent to fission, the solitons transfer some of their energy to dispersive waves (DW) propagating in the normal dispersion regime according to a phase matching condition [22]. DW generation (also known as fiber-optic Cherenkov radiation), the phenomenon responsible for generating the short-wavelength radiation in this case, has been thoroughly studied in the past [23, 24]. The supercontinuum bandwidth is dependent on the pump detuning from the ZDW, so typically one can achieve larger blue shifts in constant-diameter PCFs by using smaller core sizes, but at the expense of a spectral gap opening up between the pump and DW radiation [21]. This issue can be addressed by using a tapered geometry, where the sliding phase matching condition along the narrowing PCF can generate successively shorter wavelength DW components [16–19]. Beyond the taper waist, the spectrum stabilizes as a result of the relaxation of the light confinement and corresponding reduction in nonlinearity. This enables us to obtain a structure-free, flat band of light spanning 500-700 nm (Fig. 3c). The light is also extremely coherent ($\left|g_{12}^{(1)}\right| \approx 1$) across the whole spectral region containing significant optical power.

EXPERIMENTAL RESULTS

Following the above design, the tapered PCF was fabricated from NL-2.8-850-02 fiber by M. Harju at Vytran

LLC on a GPX-3000 series optical fiber glass processor using a heat-and-pull technique. Measurements from a micrograph of the fabricated device (Fig. 1c) agree well with the design geometry. We tested the tapered PCF by clamping it in a V-groove mount and pumping it with light from a taccor comb (Laser Quantum), recording the output spectrum on an optical spectrum analyzer (OSA). An 8 mm effective focal length aspheric lens (Thorlabs C240TME-B) was used for in-coupling, and a microscope objective (20× Olympus Plan Achromat Objective, 0.4 NA, 1.2 mm WD) was used for out-coupling. A dispersion compensation stage based on chirped mirrors was used prior to coupling to counteract the chirp induced by downstream optical elements and bring the pulse FWHM at the fiber input close to its transform limit. A half-wave plate was also inserted into the beam path before the in-coupling lens for input polarization control. Coupled power was measured with a thermal power meter just after the out-coupling microscope objective. Light was coupled into the OSA via multimode fiber (Thorlabs FG050LGA) using a fixed focus collimator (Thorlabs). We recorded spectra for a variety of femtosecond laser pump powers, optimizing the coupling before each measurement. For this series of measurements, the wave plate angle $\phi_{\lambda/2}$ was kept constant. All measurements were performed with the same equipment, the same dispersion compensation, and on the same day.

We compared our measured and simulated output spectra for the tapered PCF (Fig. 4) as a function of increasing pump power. The pulse energies shown in the right panel (simulations) were chosen to produce representative spectra. In the simulations presented here, we model the input pulse as a Gaussian with 27 fs (intensity) FWHM as this gives better agreement with measurements than the hyperbolic secant pulses used during the design stage.

In comparing simulations and measured spectra (Fig. 4), we find two principal discrepancies: (1) the simulated pulse energies are a factor of ~ 2 larger than the corresponding experimental pulse energies, and (2) there is very little radiation observed at wavelengths longer than the pump wavelength in the experimental spectra. The first discrepancy may be due to the combined effect of (geometric) out-coupling loss and reduced infrared transmission through the out-coupling objective, which is optimized for visible light; this mechanism lowers the measured out-coupled power compared to simulated spectra since the power is measured after the objective. These effects are thought to also contribute to the second discrepancy to some extent, but it is suspected that the dominant contribution comes from chromatic effects in coupling into the multimode fiber used with the OSA. Finally, there are uncertainties in fiber properties (both geometric and optical) and laser parameters (e.g., coupled bandwidth) which lead

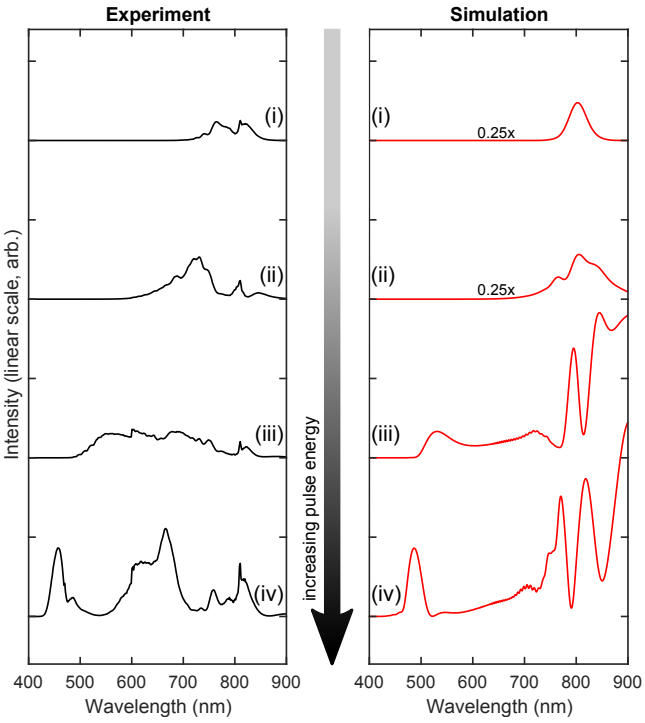


Figure 4. Comparison of experimental (left panel) and simulated (right panel) output spectra from tapered PCF pumped by taccor source comb as a function of coupled pulse energy. The spectra are offset for clarity. Except where noted, all traces within each panel have the same scale and are normalized such that the area under each curve is proportional to the pulse energy. Experimental and simulated pulse energies for each row are, respectively, (i) 24 pJ, 50 pJ, (ii) 63 pJ, 130 pJ, (iii) 100 pJ, 215 pJ, (iv) 190 pJ, 290 pJ. The discrepancies in the pulse energies and spectral features are discussed in the text.

to uncertainties in the expected spectral profiles.

Despite the differences described above, the simulations qualitatively reproduce the trend in the visible region quite well: initial symmetric broadening is followed by a wide, flat spectral plateau forming to the blue side of the pump; also, at high pump powers, the blue-shifted radiation separates into a distinct feature with a spectral gap between the pump and the dispersive waves. Experimentally, $E_p \approx 100$ pJ is an ideal operating point for an astro-comb, because it produces the flattest spectrum.

In a second test, we varied the input polarization using the half-wave plate at constant coupled pump power. The results are shown in Figure 5 (the kink in the thin green and thick blue traces near 600 nm is thought to be an artifact from the OSA). The condition denoted $\phi_{\lambda/2} = 0°$ indicates the wave plate angle that gives the flattest spectrum at $E_p = 100$ pJ (this is the angle at which all traces in the left panel of Figure 4 were recorded). At this nominal angle, the intensity variation over the 530-690 nm range is only 1.2 dB. Rotating the wave plate by 10 degrees results in a spectrum with

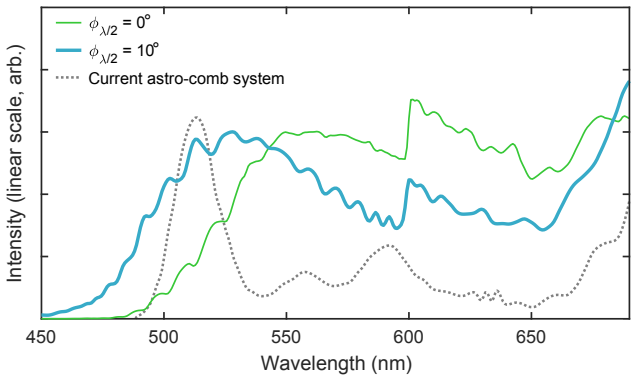


Figure 5. Measured output spectra for tapered PCF pumped by taccor source comb at different input polarizations (thin green and thick blue traces): a trade-off between spectral bandwidth and flatness is observed by rotating the input polarization using a half-wave plate at angle $\phi_{\lambda/2}$ (see text for definition). The spectra were recorded with 100 pJ coupled into the tapered PCF. The bandwidth and flatness of the green and blue traces can be compared to the PCF output spectrum from the currently deployed astro-comb system [13] (dotted gray trace).

increased bandwidth at the expense of flatness: 3.2 dB variation over 490-690 nm, with a blue tail extending below 450 nm. While the six-fold symmetry of the PCF (Fig. 1b may be responsible for the polarization dependence, the origin of this behavior is not fully understood as we use a model formulated using a single mode. A complete multi-mode formulation of the GNLSE [25] would allow us to obtain more insight into the nature of these dynamics, but this is beyond the scope of the current work.

Comparing the usable (visible) comb light from our new design to the previous-generation astro-comb, which was based on a different laser frequency comb and tapered PCF [13], our new design provides both improved bandwidth and spectral flatness. We also estimated the power per comb mode by measuring the transmission through a 10 nm-wide bandpass filter centered at 532 nm, obtaining values of $\sim 10^2$ nW/mode, which is comparable to the result in Ref. [13]. It thus satisfies the requirements for the astro-comb application. Moreover, the new tapered PCF enables the use of a turn-key Ti:sapphire laser, which greatly simplifies the astro-comb design [14]. The next step is to improve the residual dispersion of the Fabry-Perot mode filters [26] used for repetition rate multiplication, so as to preserve all of the bandwidth generated by the PCF. Another viable option would be to split the comb light into several bands and filter each band separately using narrowband cavities [27].

CONCLUSION

In summary, we demonstrated a tapered photonic crystal fiber (PCF) that produces spectrally flat light almost spanning the entire visible range when pumped by a turn-key GHz Ti:sapphire laser. Our result represents a marked improvement in the amount of optical bandwidth available to calibrate a visible-wavelength spectrograph. This work also enables a simple visible frequency comb system without the need for spectral shaping.

In addition to the calibration of astrophysical spectrographs used for Doppler velocimetry of stars, our tapered PCF design may find applications in optical coherence tomography (OCT) [8]. In OCT systems, the axial (spatial) resolution scales as $\sim \lambda_0^2/(\Delta\lambda)$, where λ_0 is the center wavelength and $\Delta\lambda$ is the bandwidth of the source. Hence, the resolution benefits from reducing the center wavelength and increasing the bandwidth, which is a similar design problem to the one addressed here. Ultrahigh-resolution visible wavelength OCT has enabled optical sectioning at the subcellular level [28] as well high-speed inspection of printed circuit boards [29]. In such applications, spectral gaps in the output band of supercontinuum sources used in OCT studies degrade the axial resolution below that possible with the full band. Thus, the spectral uniformity possible from the present tapered PCF design may improve resolution further; it may also obviate some of the challenges associated with dual-band OCT, where sophisticated signal-processing techniques are required to combine information from spectrally separated bands [30].

ACKNOWLEDGMENTS

The authors would like thank Guoquing Chang and Franz Kärtner for supplying us with the NL-2.8-850-02 photonic crystal fiber for the project, as well as for their thoughtful reading of the manuscript. A.R. would also like to thank Pawel Latawiec, Fiorenzo Omenetto, Liane Bernstein, Jennifer Schloss, Matthew Turner, Timothy Milbourne, Gábor Fűrész, and Tim Hellickson for helpful discussions.

This research work was supported by the Harvard Origins of Life Initiative, the Smithsonian Astrophysical Observatory, NASA award no. NNX16AD42G, NSF award no. AST-1405606. A.R. was supported by a postgraduate scholarship from the Natural Sciences and Engineering Research Council of Canada.

APPENDIX A: THEORETICAL MODEL

We describe the propagation of optical pulses in PCFs using the generalized nonlinear Schrödinger equation

Table I. Definitions for GNLSE model

Symbol	Definition
$*$	convolution
$\mathcal{F}\{f(T)\}$	$=\int_{-\infty}^{\infty} f(T)\,\mathrm{e}^{\mathrm{i}(\omega-\omega_0)T}\mathrm{d}T$, Fourier operator
$\mathcal{F}^{-1}\{g(\omega-\omega_0)\}$	$=(2\pi)^{-1}\int_{-\infty}^{\infty} g(\omega-\omega_0)\,\mathrm{e}^{-\mathrm{i}(\omega-\omega_0)T}\mathrm{d}\omega$, inverse Fourier operator
z	longitudinal coordinate
ω	angular frequency
t	time
ω_0	reference frequency (set to center of computational window)
ω_c	pulse carrier frequency
$\beta(\omega)$	$=n_{\mathrm{eff}}(\omega)\times\omega/c$, propagation constant
$n_{\mathrm{eff}}(\omega)$	effective index
c	speed of light in vacuum
$\beta_n(\omega)$	$=\partial^n\beta/\partial\omega^n$, n^{th}-order dispersion
T	$=t-\beta_1(\omega_c)z$, time in comoving frame
$\tilde{A}(z,\omega-\omega_0)$	spectral envelope of pulse
$A(z,T)$	$=\mathcal{F}^{-1}\left\{\tilde{A}(z,\omega-\omega_0)\right\}$, time-domain envelope of pulse
$\mathcal{D}(\omega)$	$=\mathrm{i}\left[\beta(\omega)-\beta(\omega_0)-\beta_1(\omega_c)(\omega-\omega_0)\right]-\frac{1}{2}\alpha(\omega)$, dispersion operator
$\alpha(\omega)$	frequency-dependent loss
$\tilde{A}_I(z,\omega-\omega_0)$	$=\mathrm{e}^{-\mathcal{D}(\omega)z}\tilde{A}(z,\omega-\omega_0)$, interaction picture spectral envelope of pulse
$\bar{\gamma}(\omega)$	$=\frac{n_2 n_{\mathrm{eff}}(\omega_0)\omega}{c n_{\mathrm{eff}}(\omega)A_{\mathrm{eff}}^{1/4}(\omega)}$, frequency-dependent nonlinear parameter
n_2	nonlinear refractive index
$A_{\mathrm{eff}}(\omega)$	$=\frac{\left(\int_{-\infty}^{\infty}\int_{-\infty}^{\infty}\lvert F(x,y,\omega)\rvert^2 dxdy\right)^2}{\int_{-\infty}^{\infty}\int_{-\infty}^{\infty}\lvert F(x,y,\omega)\rvert^4 dxdy}$, frequency-dependent mode effective area
$F(x,y,\omega)$	transverse modal distribution
$\bar{A}(z,T)$	$=\mathcal{F}^{-1}\left\{\tilde{A}(z,\omega-\omega_0)/A_{\mathrm{eff}}^{1/4}(\omega)\right\}$
$R(t)$	$=(1-f_r)\delta(t)+f_r h_r(t)\Theta(t)$, Raman response function
f_r	fractional contribution of delayed Raman response
$h_r(t)$	$=\frac{\tau_1^2+\tau_2^2}{\tau_1\tau_2^2}\exp(-t/\tau_2)\sin(t/\tau_1)$, with Raman fit parameters τ_1,τ_2
$\Theta(t)$	Heaviside function

(GNLSE). Here, we work in the interaction picture and use a frequency domain formulation, following Ref. [31]. The GNLSE [21] is expressed as

$$\frac{\partial}{\partial z}\tilde{A}_I = \mathrm{i}\bar{\gamma}(\omega)\exp(-\mathcal{D}(\omega)z) \times\mathcal{F}\left\{\bar{A}(z,T)\times\left(R(T)*\left|\bar{A}(z,T)\right|^2\right)\right\}. \quad (1)$$

Table I summarizes the definitions of all the symbols used above.

In terms of the GNLSE, the PCF is entirely described by $\mathcal{D}(\omega)$, $\bar{\gamma}(\omega)$ and $R(t)$. The fiber material is fused silica, so we take $f_r = 0.18$, $\tau_1 = 12.2$ fs, and $\tau_2 = 32$ fs as given in Ref. [32], and $n_2 \approx 2.5\times10^{-20}$ m^2/W [33] for all our calculations. We neglect any losses, i.e., $\alpha(\omega)=0$.

Note that in tapered geometries, both the dispersion operator and the frequency-dependent nonlinear parameter become functions of z as well, i.e., $\mathcal{D}(\omega)\to\mathcal{D}(\omega,z)$ and $\bar{\gamma}(\omega)\to\bar{\gamma}(\omega,z)$ [34, 35]. This approach has been pointed out to not be strictly correct as it does not conserve the photon number [20, 36], but we have adopted it here for simplicity. Our solver codes are available upon request.

APPENDIX B: CALCULATION OF SUPERCONTINUUM COHERENCE

We use a first-order measure $g_{12}^{(1)}$ to evaluate the coherence [7] of the output optical field $\tilde{A}(\omega)$ from the PCF,

$$\left|g_{12}^{(1)}(\omega)\right| = \frac{\left|\left\langle\tilde{A}_i^*(\omega)\,\tilde{A}_j(\omega)\right\rangle_{i\neq j}\right|}{\sqrt{\left\langle\left|\tilde{A}_i(\omega)\right|^2\right\rangle\left\langle\left|\tilde{A}_j(\omega)\right|^2\right\rangle}} \quad (2)$$

where $\langle\cdots\rangle$ is an ensemble average over N propagations of the simulation.

Each run of the simulation differs by some noise injected into the input field. We include only a shot noise seed and no spontaneous Raman noise, as shot noise has

been shown to be the dominant noise process [37]. To perturb the input pulse (in the time domain), we follow Ref. [38, 39]: to each temporal bin of both the real and imaginary components of A, we add a random number drawn from a normal distribution with zero mean and variance $\hbar\omega/(4\Delta T)$, where ω is the pulse average frequency and ΔT is the temporal bin width. In Figure 3c, we evaluate $\left|g_{12}^{(1)}\right|$ over $N = 100$ runs of the simulation.

* aravi@physics.harvard.edu

[1] D. A. Fischer, G. Anglada-Escude, P. Arriagada, R. V. Baluev, J. L. Bean, F. Bouchy, L. A. Buchhave, T. Carroll, A. Chakraborty, J. R. Crepp, *et al.*, Publ. Astron. Soc. Pac. **128**, 066001 (2016).

[2] M. Mayor, F. Pepe, D. Queloz, F. Bouchy, G. Rupprecht, G. Lo Curto, G. Avila, W. Benz, J.-L. Bertaux, X. Bonfils, *et al.*, The Messenger **114**, 20 (2003).

[3] R. Cosentino, C. Lovis, F. Pepe, A. C. Cameron, D. W. Latham, E. Molinari, S. Udry, N. Bezawada, M. Black, A. Born, *et al.*, Proc. SPIE **8446**, 84461V (2012).

[4] R. A. McCracken, J. M. Charsley, and D. T. Reid, Opt. Express **25**, 15058 (2017).

[5] A. J. Benedick, G. Chang, J. R. Birge, L.-J. Chen, A. G. Glenday, C.-H. Li, D. F. Phillips, A. Szentgyorgyi, S. Korzennik, G. Furesz, R. L. Walsworth, and F. X. Kärtner, Opt. Express **18**, 19175 (2010).

[6] D. F. Phillips, A. G. Glenday, C.-H. Li, C. Cramer, G. Furesz, G. Chang, A. J. Benedick, L.-J. Chen, F. X. Kärtner, S. Korzennik, D. Sasselov, A. Szentgyorgyi, and R. L. Walsworth, Opt. Express **20**, 13711 (2012).

[7] J. M. Dudley, G. Genty, and S. Coen, Rev. Mod. Phys. **78**, 1135 (2006).

[8] I. Hartl, X. D. Li, C. Chudoba, R. K. Ghanta, T. H. Ko, J. G. Fujimoto, J. K. Ranka, and R. S. Windeler, Opt. Lett. **26**, 608 (2001).

[9] D. J. Jones, S. A. Diddams, J. K. Ranka, A. Stentz, R. S. Windeler, J. L. Hall, and S. T. Cundiff, Science **288**, 635 (2000).

[10] T. Wilken, G. Lo Curto, R. A. Probst, T. Steinmetz, A. Manescau, L. Pasquini, J. I. González Hernández, R. Rebolo, T. W. Hänsch, T. Udem, and R. Holzwarth, Nature **485**, 611 (2012).

[11] R. A. Probst, T. Steinmetz, T. Wilken, G. K. L. Wong, H. Hundertmark, S. P. Stark, P. S. J. Russell, T. W. Hänsch, R. Holzwarth, and T. Udem, Proc. SPIE **8864**, 88641Z (2013).

[12] R. A. McCracken, É. Depagne, R. B. Kuhn, N. Erasmus, L. A. Crause, and D. T. Reid, Opt. Express **25**, 6450 (2017).

[13] A. G. Glenday, C.-H. Li, N. Langellier, G. Chang, L.-J. Chen, G. Furesz, A. A. Zibrov, F. Kärtner, D. F. Phillips, D. Sasselov, A. Szentgyorgyi, and R. L. Walsworth, Optica **2**, 250 (2015).

[14] A. Ravi, D. F. Phillips, M. Beck, L. L. Martin, M. Cecconi, A. Ghedina, E. Molinari, A. Bartels, D. Sasselov, A. Szentgyorgyi, and R. L. Walsworth, J. Astron. Telesc. Instrum. Syst. **3**, 045003 (2017).

[15] R. A. Probst, G. Lo Curto, G. Avila, B. L. Canto Martins, J. Renan De Medeiros, M. Esposito, J. I. González Hernández, T. W. Hänsch, R. Holzwarth, F. Kerber, *et al.*, Proc. SPIE **9147**, 91471C (2014).

[16] F. Lu, Y. Deng, and W. H. Knox, Opt. Lett. **30**, 1566 (2005).

[17] F. Lu and W. H. Knox, J. Opt. Soc. Am. B **23**, 1221 (2006).

[18] A. Kudlinski, A. K. George, J. C. Knight, J. C. Travers, A. B. Rulkov, S. V. Popov, and J. R. Taylor, Opt. Express **14**, 5715 (2006).

[19] P. Pal, W. H. Knox, I. Hartl, and M. E. Fermann, Opt. Express **15**, 12161 (2007).

[20] J. Lægsgaard, J. Opt. Soc. Am. B **29**, 3183 (2012).

[21] J. M. Dudley and J. R. Taylor, eds., *Supercontinuum Generation in Optical Fibers* (Cambridge University Press, 2010).

[22] N. Akhmediev and M. Karlsson, Phys. Rev. A **51**, 2602 (1995).

[23] G. Chang, L.-J. Chen, and F. X. Kärtner, Opt. Lett. **35**, 2361 (2010).

[24] G. Chang, L.-J. Chen, and F. X. Kärtner, Opt. Express **19**, 6635 (2011).

[25] F. Poletti and P. Horak, J. Opt. Soc. Am. B **25**, 1645 (2008).

[26] L.-J. Chen, G. Chang, C.-H. Li, A. J. Benedick, D. F. Philips, R. L. Walsworth, and F. X. Kärtner, Opt. Express **18**, 23204 (2010).

[27] D. A. Braje, M. S. Kirchner, S. Osterman, T. Fortier, and S. A. Diddams, Eur. Phys. J. D **48**, 57 (2008).

[28] P. J. Marchand, A. Bouwens, D. Szlag, D. Nguyen, A. Descloux, M. Sison, S. Coquoz, J. Extermann, and T. Lasser, Biomed. Opt. Express **8**, 3343 (2017).

[29] J. Czajkowski, J. Lauri, R. Sliz, P. Fält, T. Fabritius, R. Myllylä, and B. Cense, Proc. SPIE **8430**, 84300K (2012).

[30] P. Cimalla, M. Gaertner, J. Walther, and E. Koch, Proc. SPIE **8213**, 82132M (2012).

[31] J. Hult, J. Lightwave Technol. **25**, 3770 (2007).

[32] G. Agrawal, *Nonlinear Fiber Optics*, 5th ed. (Academic Press, 2012).

[33] Crystal Fibre A/S, NL-2.8-850-02 datasheet.

[34] J. C. Travers and J. R. Taylor, Opt. Lett. **34**, 115 (2009).

[35] A. C. Judge, O. Bang, B. J. Eggleton, B. T. Kuhlmey, E. C. Mägi, R. Pant, and C. M. de Sterke, J. Opt. Soc. Am. B **26**, 2064 (2009).

[36] O. Vanvincq, J. C. Travers, and A. Kudlinski, Phys. Rev. A **84**, 063820 (2011).

[37] K. L. Corwin, N. R. Newbury, J. M. Dudley, S. Coen, S. A. Diddams, K. Weber, and R. S. Windeler, Phys. Rev. Lett. **90**, 113904 (2003).

[38] R. Paschotta, Appl. Phys. B **79**, 153 (2004).

[39] A. Ruehl, M. J. Martin, K. C. Cossel, L. Chen, H. McKay, B. Thomas, C. Benko, L. Dong, J. M. Dudley, M. E. Fermann, I. Hartl, and J. Ye, Phys. Rev. A **84**, 011806 (2011).